Volume 7
Number 18
21 September 2025
Pages 5439–5830

Nanoscale Advances

rsc.li/nanoscale-advances

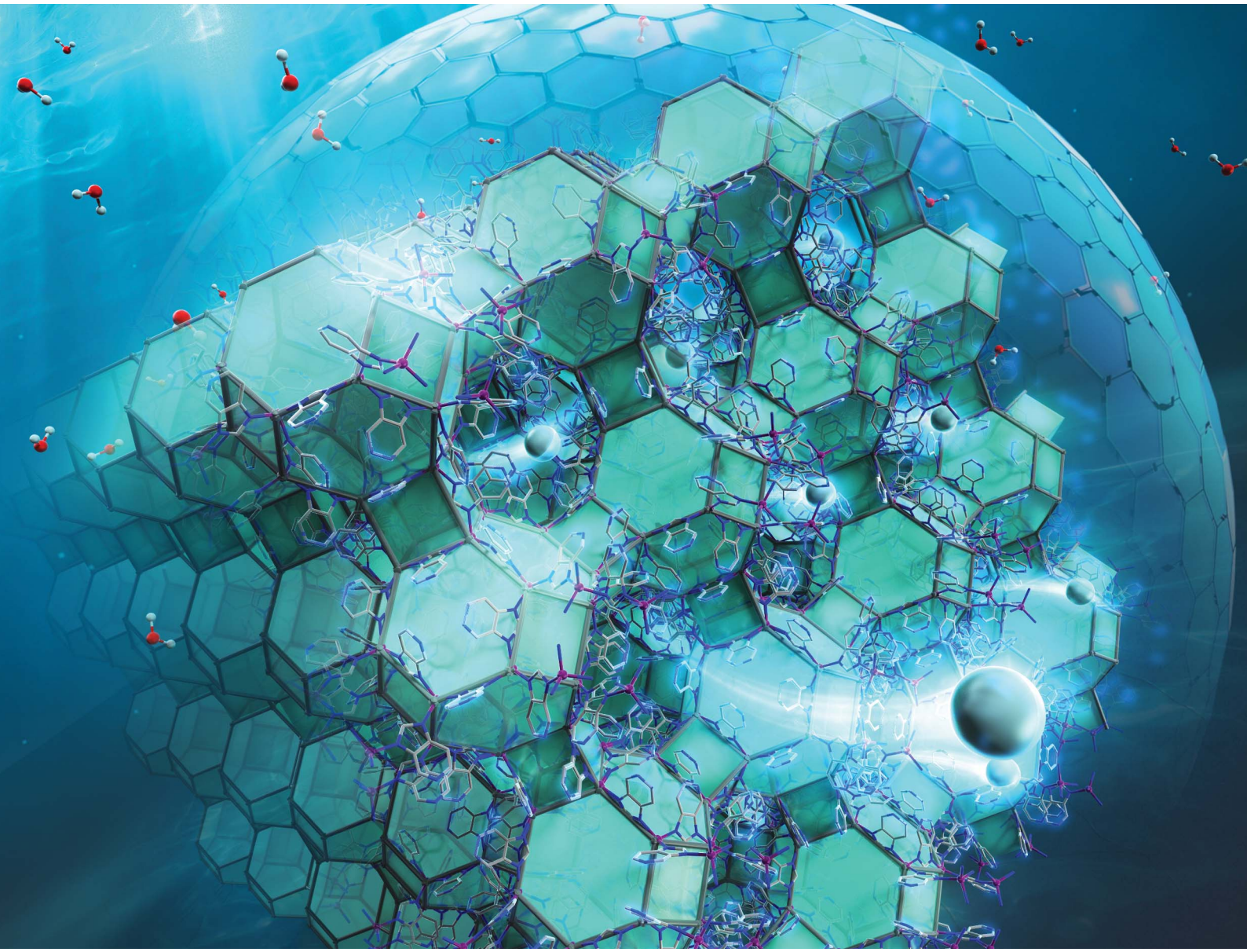

ISSN 2516-0230

ROYAL SOCIETY OF CHEMISTRY

PAPER
Hiroi Sei, Kouki Oka *et al.*
Zeolitic imidazolate framework-22: high hydrophilicity, water resistance, and proton conduction

NCNST

Nanoscale Advances

ROYAL SOCIETY OF CHEMISTRY

PAPER

View Article Online
View Journal | View Issue

Cite this: *Nanoscale Adv.*, 2025, **7**, 5501

Zeolitic imidazolate framework-22: high hydrophilicity, water resistance, and proton conduction

Hiroi Sei, *[a] Hitoshi Kasai [a] and Kouki Oka *[abc]

Among metal–organic frameworks (**MOF**s), zeolitic imidazolate frameworks (**ZIF**s) enable precise design of pore structures, and most of them exhibit high water resistance. However, no hydrophilic **ZIF** that maintains water resistance and adsorbs water vapor in low-pressure range has been achieved. In the current work, as a **MOF** with both high structural stability and hydrophilicity, we focused on **ZIF-22** that contains one polar uncoordinated *N*-heteroatom in its organic linker. **ZIF-22** exhibited high water resistance due to presence of an appropriate number (one) of uncoordinated *N*-heteroatoms. The added polarity from *N*-heteroatoms allowed **ZIF-22** to exhibit the highest hydrophilicity among **ZIF**s. Furthermore, **ZIF-22** exhibited the highest proton conductivity (1.77×10^{-3} S cm^{-1} at 363 K and 95% RH) among **ZIF**s without acidic groups or guest proton carriers. These findings provide a design strategy of **MOF**s that achieve hydrophilization while maintaining water resistance and broaden their application range in aqueous environments.

Received 17th July 2025
Accepted 1st August 2025

DOI: 10.1039/d5na00686d

rsc.li/nanoscale-advances

Introduction

Metal–organic frameworks (**MOF**s) enable the design of various porous structures *via* the combination of metal ions and organic linkers,[1] and therefore various applications such as the separation of gas molecules,[2–4] sensing,[5–7] catalytic reactions,[8] and proton conduction,[9,10] have been developed. In most applications, water and moisture are present in the environment, and contact with water is unavoidable; therefore, functionalization in aqueous environments is an important research topic.[11,12] However, water tends to undergo hydrolysis of coordination bonds between metal ions and organic linkers and usually reduces the structural stability of **MOF**s.[13–15] Therefore, for the functional development in aqueous environments, construction of water-resistant **MOF**s is essential. Furthermore, in water-resistant **MOF**s, the ease of access of water molecules to the pores influences their performance;[16,17] therefore, their hydrophilicity is also important. The hydrophilicity of **MOF**s is evaluated *via* the adsorption properties of water vapor in the low-pressure range[18] and increases with a lower pore filling pressure.

Zeolitic–Imidazolate Frameworks (**ZIF**s) are cage-like **MOF**s composed of metal ions and imidazole derivatives;[19] the coordination bond is relatively strong;[20] therefore, a number of **ZIF**s exhibit water resistance,[21,22] and their functional development in aqueous environments is expected.[20,23,24] Furthermore, the molecular design of imidazole derivatives[25] enables more precise control of pore sizes (windows and inner pores) among **MOF**s *via* the network topology that is the style of linkage between metal ions and organic linkers, and porous structures based on more than 40 different network topologies[19,26] have been reported as **ZIF**s.[22,25] However, most water-resistant **ZIF**s adsorb little water vapor even near the saturated pressure[21,27,28] and exhibit very strong hydrophobicity. The strong hydrophobicity of **ZIF**s reduces the uptake of water molecules into the pores, which causes poor performances[29,30] and limits the applications of **ZIF**s in aqueous environments.

Toward hydrophilization of **ZIF**s, the introduction of polar functional groups into imidazole derivatives has been attempted.[31] Although **ZIF-90** had protic aldehyde groups at the 2-position on imidazolate and formed the same **SOD** topology as the strongly hydrophobic **ZIF-8**, owing to the reduction in the hydrophobicity of **ZIF**s by the aldehyde groups, **ZIF-90** dramatically adsorbed water vapor at 0.3–0.4 P/P_0,[27] and amphiphilicity was reported.[32] However, the introduction of other polar functional groups, such as nitro and amino groups, into **ZIF**s decreases the pK_a of the organic linker, weakens the coordination bond between the metal ion and imidazole, and usually reduces water resistance.[33] Therefore, **ZIF**s with hydrophilicity and water resistance are few, and highly hydrophilic **ZIF**s that can adsorb water vapor in the low-pressure range ($0 < P/P_0 < 0.1$) have not been achieved.

In **MOF**s, the introduction of uncoordinated *N*-heteroatom sites, such as the N atom of pyridine, does not change the pore volume but provides polarity to the pore surface, which

[a]*Institute of Multidisciplinary Research for Advanced Materials, Tohoku University, 2-1-1 Katahira, Aoba-ku, Sendai, Miyagi 980-8577, Japan. E-mail: hiroi.sei.a8@tohoku.ac.jp; oka@tohoku.ac.jp*

[b]*Center for the Promotion of Interdisciplinary Education and Research, Kyoto University, Yoshida-honmachi, Sakyo-ku, Kyoto 606-8501, Japan*

[c]*Carbon Recycling Energy Research Center, Ibaraki University, Hitachi, 4-12-1 Nakanarusawacho, Ibaraki 316-0033, Japan*

improves hydrophilicity.[34,35] Prof. B. Li *et al.* introduced three types of hydrophilic groups—amino groups (**UiO-66-NH$_2$**), hydroxy groups (**UiO-66-OH**), and *N*-heteroatom sites (**UiO-66-N**)—into **UiO-66** and reported that **UiO-66-N** adsorbed water vapor at the lowest pressure among them; therefore, *N*-heteroatom sites enhanced the hydrophilicity more than the other functional groups.[34] In contrast, an increase in the number of *N*-heteroatoms in an organic linker decreases the pK_a,[36] which weakens the coordination bonds and reduces the water resistance of the **MOF**s.[37–39] Thus, when **MOF**s are hydrophilized through the introduction of uncoordinated *N*-heteroatom sites, the number of *N*-heteroatoms should be optimized to maintain water resistance, but hydrophilicity and water resistance have not been investigated simultaneously.

In the current work, to elucidate an appropriate number of uncoordinated *N*-heteroatoms in **ZIF**s, we focused on **ZIF-20** (ref. 40) and **ZIF-22** (ref. 40) which have the same network topology (**LTA**) but different numbers of uncoordinated *N*-heteroatoms in the organic linker (Fig. 1a). The previous paper[41] shows that **ZIF-20**, which uses purine with two uncoordinated *N*-heteroatoms as an organic linker, changed its structure upon exposure to water and exhibited low water resistance (Fig. 1a). The current work demonstrated that **ZIF-22** with one uncoordinated *N*-heteroatom in an organic linker (Fig. 1b) possessed an appropriate number of uncoordinated *N*-heteroatoms; therefore, maintained structural stability and had a polar pore surface, which led to the achievement of both water resistance and high hydrophilicity (Fig. 1b).

Results and discussion

ZIF-22 was prepared according to Prof. D. W. Park *et al.*[42] (see SI: preparation of **ZIF-22**). **ZIF-20** was also prepared according to Prof. O. M. Yaghi *et al.*[40] (see SI: preparation of **ZIF-20**). The powder X-ray diffraction (**PXRD**) pattern of the crystal immediately following formation was identical to the simulated pattern of **ZIF-22** (Fig. S1), which indicated the successful construction of **ZIF-22**. **ZIF-22** was activated by evacuation *in vacuo* at 80 °C for 3 h after drying with supercritical CO_2 fluid. The **FT-IR** spectrum of activated **ZIF-22** (Fig. S2, red) showed no peak corresponding to the C=O stretching mode of DMF (Fig. S2, black, 1660 cm^{-1}) or the C–N stretching mode of the uncoordinated organic linker (Fig. S2, blue, 1124 cm^{-1}). Moreover, **NMR** measurements (Fig. S3) of activated **ZIF-22** confirmed that the organic solvents used for its preparation were removed, which supported that **ZIF-22** was sufficiently activated. The activated **ZIF-22** showed a 13% weight loss (Fig. S4) up to 400 °C, but no organic solvents or uncoordinated organic linkers were present, which indicated that the weight loss was caused by water. Furthermore, the **PXRD** pattern of activated **ZIF-22** (Fig. S1) was identical to that of **ZIF-22** immediately following formation, which indicated that the activated **ZIF-22** maintained its original structure.

We performed N_2 and CO_2 gas adsorption measurements of **ZIF-22** and its porosity was examined. The N_2 adsorption capacities of **ZIF-22** were 3.1 mL g^{-1} (77 K, P/P_0 = 0.9) and 0.017 mL g^{-1} (298 K, P/P_0 = 0.9), which indicated that **ZIF-22** scarcely adsorbed N_2 (Fig. S5). This indicated that the window of **ZIF-22** (3.0 Å)[43] was narrower than the kinetic diameter of N_2 (3.8 Å),[2] and therefore N_2 did not pass through the window by molecular sieving effect. In contrast, the kinetic diameter of CO_2 (3.3 Å)[2] was larger than the size of the window, but **ZIF-22** adsorbed 11 mL g^{-1} CO_2 at 298 K (Fig. S5a). Previous investigation[44] reported that in the case of **ZIF-8**, a representative **ZIF**, due to the rotation of the organic linker, the effective window size (4.0 to 4.2 Å)[44] was larger than that of the window (3.4 Å)[44] that was determined by crystal structure. This indicates that, in the case of **ZIF-22**, the rotation of the organic linker enables the adsorption of CO_2 with a slightly smaller kinetic diameter than the effective window size of **ZIF-22**. From the above, activated **ZIF-22** maintained its porosity.

ZIF-22 immediately following formation was soaked in pure water at 298 K for 7 days, and its water resistance was examined. As shown in Fig. 2a, the **PXRD** pattern of **ZIF-22** after soaking in water was identical to that obtained immediately following formation. Previous papers[45,46] indicated that hydrolysis of **ZIF**s formed Zn–OH bonds, and the bond formation increased the binding energy of Zn in X-ray photoelectron spectroscopy (**XPS**). However, Zn 2p$_{3/2}$ **XPS** spectra (Fig. S6) showed that the peak of Zn in **ZIF-22** after soaking in water was identical to that in activated **ZIF-22**, and therefore, the hydrolysis of **ZIF-22** did not occur. These **PXRD** patterns and **XPS** spectra exhibited their high water resistance. A previous investigation[41] reported that in **LTA**-type **ZIF-20** using purine as the organic linker, the structure was changed *via* water soaking, and therefore the water resistance was low. As **ZIF-22** has the same network topology as **ZIF-20**,[40] the difference in water resistance can be attributed to the strength of the coordination bonds between the Zn ions and organic linkers. The lower pK_a of the organic linker decreases the basicity and electron density of the

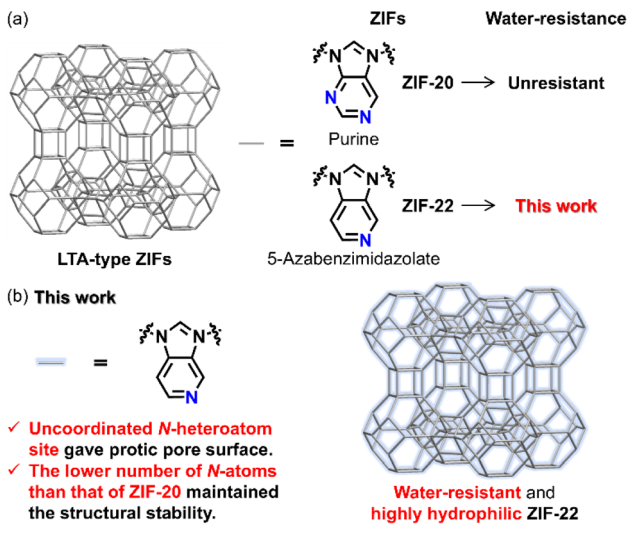

Fig. 1 (a) Schematic representation of the structure of LTA-type ZIF-20 and ZIF-22, and the chemical structure of their organic linkers. (b) Water-resistant and hydrophilic ZIF-22 composed of 5-azabenzimidazole with a lower number of hydrophilic uncoordinated *N*-heteroatom sites than that of ZIF-20.

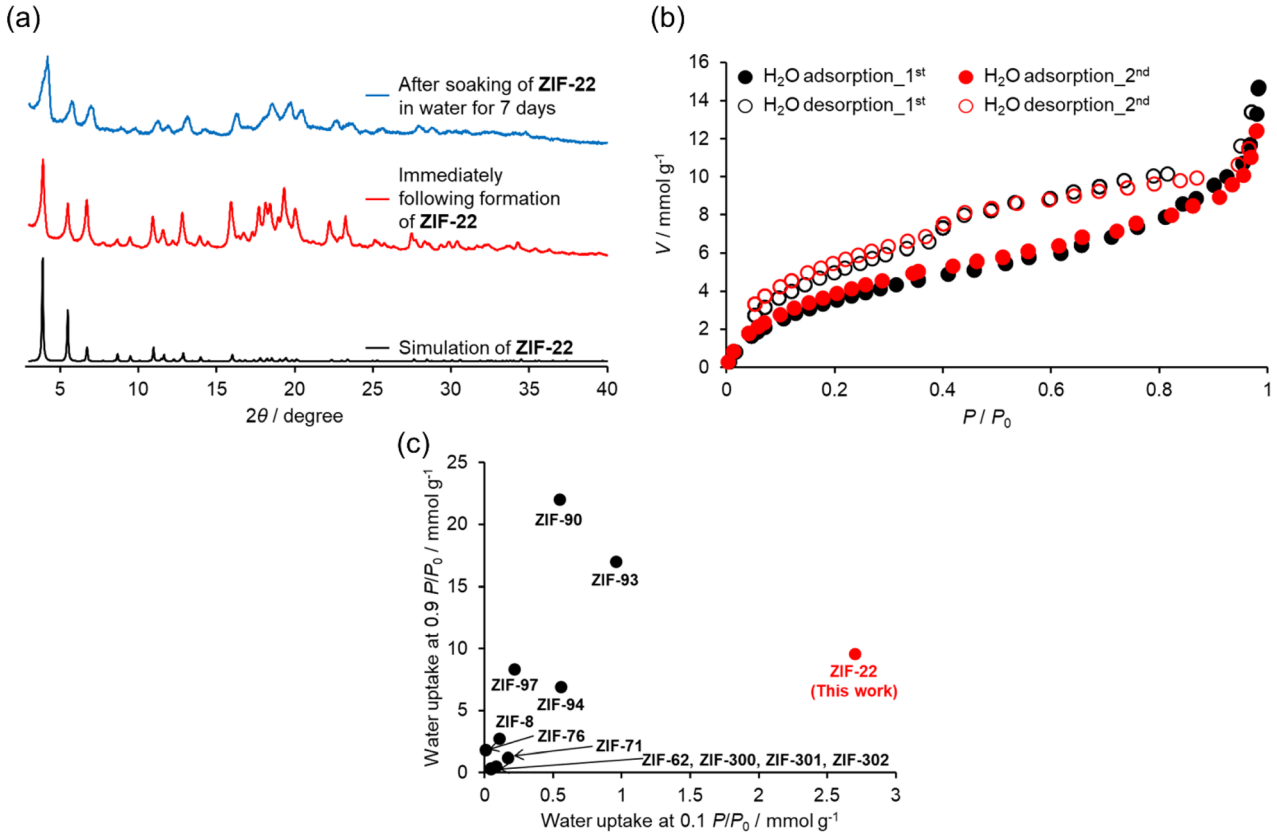

Fig. 2 (a) PXRD patterns of ZIF-22: simulation (black), immediately following formation of ZIF-22 (red), and after soaking of ZIF-22 in water (298 K) for 7 days (blue). (b) Water adsorption isotherms of ZIF-22 at 298 K. Filled symbols: adsorption process, open symbols: desorption process. P denotes the pressure at adsorption and P_0 denotes the condensation pressure of the adsorbate at the measurement temperature. (c) Distribution map of water uptakes at 0.9 P/P_0 with corresponding water uptakes at 0.1 P/P_0 in ZIFs.

conjugate base, which usually weakens the coordination bond between the metal ion and the organic linker.[37] The pK_a values of the organic linkers and benzimidazole with no uncoordinated *N*-heteroatom were determined by density-functional-theory (**DFT**) calculations. As shown in Table S1, the pK_a value decreased with increasing number of N atoms, and the pK_a value of purine (pK_a (calc.) = 8.0) was lower than that of 5-azabenzimidazole (pK_a (calc.) = 10.5). Conjugated bases of organic linkers with high electronegativities exhibit high basicities and electron densities, resulting in the formation of strong coordination bonds.[37] In **XPS** measurement, the formation of chemical bonds with electronegative atoms shifts the binding energy of core electrons to a higher value.[47,48] Zn $2p_{3/2}$ **XPS** spectra (Fig. S7) that relate to their coordination bonds showed that the binding energy of **ZIF-22** (1021.9 eV) was higher than that of **ZIF-20** (1021.6 eV), which indicated that the electronegativity of 5-azabenzimidazolate was higher than that of purinate, and the Zn–N bond of **ZIF-22** was stronger than that of **ZIF-20**. Therefore, in the case of **ZIF-20**, the presence of many N atoms (two uncoordinated heteroatoms per organic linker) in purine reduced the pK_a and weakened the coordination bond between the Zn ions and the organic linker; therefore, its water resistance was reduced. In contrast, because **ZIF-22** contains only one uncoordinated *N*-heteroatom in 5-azabenzimidazole, the coordination bond is not significantly weakened; therefore, **ZIF-22** exhibited water-resistance.

The water vapor adsorption property of **ZIF-22** was measured to examine its hydrophilicity. In the case of **ZIF-20**, previous papers[41,49] indicated that the structure collapsed upon water soaking, and therefore the water vapor adsorption property of **ZIF-20** could not be measured. Fig. 2b showed the adsorption isotherm of water vapor at 298 K. **ZIF-22** adsorbed 9.6 mmol g^{-1} of water vapor at 0.9 P/P_0 and exhibited a type-II isotherm where an adsorption uptake was increased from 0 P/P_0. A previous investigation[50] reported that **ZIF-76**, which uses nonpolar imidazole and 5-chlorobenzimidazole as organic linkers and has the same **LTA** topology as **ZIF-22**, adsorbed only 1.8 mmol g^{-1} of water vapor at 0.9 P/P_0 and began adsorption only near the saturated pressure ($0.8 < P/P_0 < 0.9$) and had hydrophobicity. Therefore, the polarity of the uncoordinated *N*-heteroatom sites on the pore surface of **ZIF-22** enhanced its hydrophilicity.

The hydrophilicity of **MOF**s increases with a lower pore filling pressure for water vapor;[18] therefore, we compared the adsorption uptakes for water vapor at 0.1 P/P_0 in reported **ZIF**s (Table S2). As shown in Fig. 2c, the adsorption uptake of **ZIF-22** for water vapor at 0.1 P/P_0 (2.7 mmol g^{-1}) was the highest among the reported **ZIF**s, which indicated that **ZIF-22** is the most hydrophilic among them. The pore filling pressure of **ZIF-**

22 (<0.1 P/P_0) was lower than that of representative water-stable **MOF**s like **UiO-66** (0.36 P/P_0)[51] and **MIL-101** (0.46 P/P_0),[51] which indicated that **ZIF-22** was more hydrophilic than their **MOF**s. Furthermore, the water vapor adsorption isotherm of **ZIF-22** was measured continuously (Table S3). The adsorption isotherm of the first measurement (Fig. 2b, black) was identical to that of the second measurement (Fig. 2b, red), and the adsorption uptake did not decrease. In the **PXRD** pattern of **ZIF-22** (Fig. S8) after water vapor adsorption, the peak positions remained unchanged. Moreover, the CO_2 adsorption capacity of **ZIF-22** after water vapor adsorption was almost the same as that of **ZIF-22** before water vapor adsorption (Table S4). Therefore, both the **PXRD** and adsorption measurements demonstrated the high water resistance of **ZIF-22**. These results supported the idea that one uncoordinated *N*-heteroatom in the organic linker of **ZIF-22** provided polarity on the pore surface without significantly weakening the coordination bond between the Zn ion and the organic linker, which resulted in both water resistance and hydrophilicity.

ZIF-22 accommodated many water molecules that act as proton sources and mediated proton transfer into the pores; therefore, proton conduction was expected. As shown in Fig. 3, the proton conductivity of the pelletized **ZIF-22** was measured by electrochemical impedance spectroscopy (**EIS**). Proton conductivity was determined *via* fitting analysis, which assumed the equivalent circuit shown in Fig. S9. As shown in Fig. 3a, at 298 K and 95% RH, the Nyquist plot of **ZIF-22** displayed a semicircle at high frequencies, and the proton conductivity of **ZIF-22** was 5.54×10^{-8} S cm^{-1}. From the direct current (**DC**) resistance measurement (Fig. S10), the **DC** electrical conductivity of **ZIF-22** at 298 K was 8.34×10^{-12} S cm^{-1}. This conductivity was four orders of magnitude lower than 5.54×10^{-8} S cm^{-1}, which confirmed that the observed conduction was due to proton conduction at 298 K and 95% RH. In the **PXRD** pattern of **ZIF-22** (Fig. S11) after the impedance measurement, the peak intensity was lower than that before the measurement, but the peak positions remained unchanged. Moreover, Zn $2p_{3/2}$ **XPS** spectra (Fig. S6) showed that the peak of Zn in **ZIF-22** after the impedance measurement was identical to that in activated **ZIF-22**, and therefore, the hydrolysis of **ZIF-22** did not occur during the impedance measurement. These results indicated that the porous structure was maintained.

Because the proton conductivity usually increases with increasing temperature[52] as shown in Fig. 3a and Fig. S12, we measured the proton conductivities of **ZIF-22** at different temperatures (298, 303, 323, 333, 343, 353, and 363 K). As shown in Table S5, the proton conductivity of **ZIF-22** dramatically increased with increasing temperature from 5.54×10^{-8} S cm^{-1} at 298 K to 1.77×10^{-3} S cm^{-1} at 363 K. This proton conductivity was the highest among **ZIF**s without acidic groups or guests as proton carriers (Table S6). Previous paper[53] indicated that in proton conductive **MOF**s, the high proton conductivity is above 10^{-3} S cm^{-1}. Therefore, the proton conductivity of **ZIF-22** (1.77×10^{-3} S cm^{-1} at 363 K and 95% RH) is comparable to other **MOF**s with high proton conductivities. The window sizes of both **ZIF-22** (3.0 Å)[43] and **ZIF-8** (3.4 Å),[29] representative **ZIF**s, are relatively similar to the size of a H_3O^+ ion (2.0 Å),[54] and **ZIF-22** has a narrower window than that of **ZIF-8**. The narrow window would disrupt the dispersion of H_3O^+ ions. Therefore, in the case of proton conduction with a vehicle mechanism[9,55] where H_3O^+ ions directly move in the pore, the structure of **ZIF-22** is more unfavorable for proton conduction. However, the proton conductivity of **ZIF-22** (1.8×10^{-3} S cm^{-1} at 363 K and 95% RH) was higher than that of hydrophobic **ZIF-8** (4.6×10^{-4} S cm^{-1} at 367 K and 98% RH),[29] which supported that uncoordinated *N*-heteroatoms in **ZIF-22** accommodated more water molecules into the pore, increased the number of proton carriers, and enhanced proton conductivity. **ZIF-90** adsorbs water vapor at 0.9 P/P_0 (Table S2) as well as **ZIF-22**, but the size of the inner pore of the cage (11.2 Å)[32] is smaller than that of **ZIF-22** (18.2 Å). A larger pore size is favorable for proton conduction at high temperature and humidity,[56] which supported the idea that the proton conductivity of **ZIF-22** was higher than that of **ZIF-90** (1.9×10^{-4} S cm^{-1} at 373 K and 98% RH).[57]

As shown in the Arrhenius plots in Fig. 3b, the activation energy was 1.6 eV, larger than 0.4 eV, which indicated that proton conduction in **ZIF-22** mainly follows a vehicle mechanism. Previous investigation[29] reported that the narrow window (3.4 Å) of **ZIF-8** disturbed proton transfer and resulted in the high activation energy (1.1 eV) of proton conduction. Therefore,

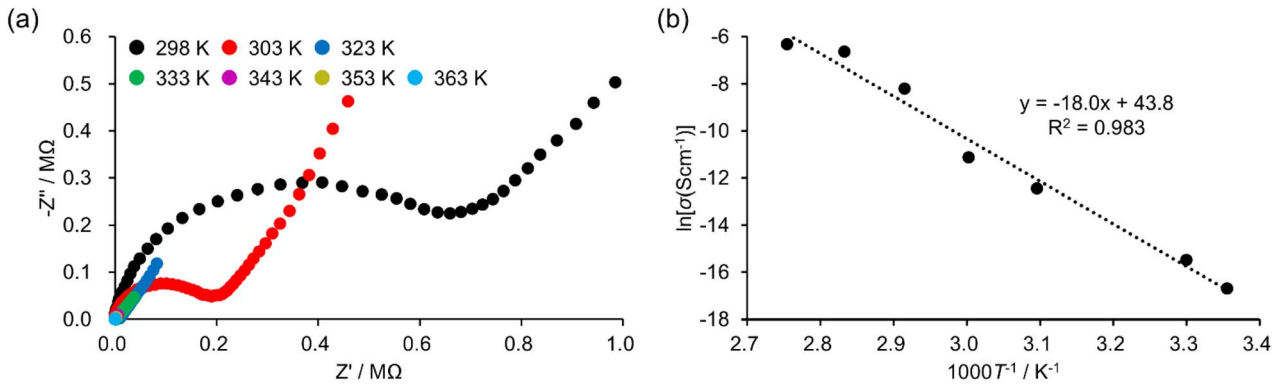

Fig. 3 Impedance spectra (a) and Arrhenius plots of conductivity (b) for the disk-shaped pellets of **ZIF-22** under 95% RH at 298, 303, 323, 333, 343, 353, and 363 K.

the narrower window (3.0 Å) of **ZIF-22** disrupted the dispersion of H_3O^+ ions, which resulted in high activation energy.

Conclusions

The effects of introducing uncoordinated *N*-heteroatom sites on both hydrophilicity and water resistance were simultaneously investigated, and an optimized number of *N*-heteroatoms to achieve both high hydrophilicity and maintenance of structural stability was revealed in **MOF**s for the first time. **ZIF-22**, with one polar uncoordinated *N*-heteroatom in the organic linker, maintained its crystal structure even after soaking in water (298 K) for 7 days, which exhibited high water resistance. Furthermore, **ZIF-22** adsorbed 9.6 mmol g^{-1} ($P/P_0 = 0.9$) of water at 298 K, and water vapor adsorption commenced at 0 P/P_0, which indicated that **ZIF-22** was the most hydrophilic among **ZIF**s. Moreover, **ZIF-22** accommodated more water molecules (2.9 water molecules/Zn(5-azabenzimidazole)$_2$) into the pores, and therefore, exhibited a proton conductivity of 1.77×10^{-3} S cm^{-1} (363 K, 95% RH). These findings provide a design strategy of **MOF**s that achieve hydrophilization while maintaining water resistance and broaden their application range in aqueous environments.

Author contributions

K. O. conceived and supervised the project. H. S. and K. O. designed the research and performed synthesis, characterization, proton conductivity measurements, and other major experiments. H. S. and K. O. wrote the initial draft of the paper, and all authors contributed to the editing of the paper. All authors have approved the final version of the manuscript.

Conflicts of interest

There are no conflicts of interest to declare.

Data availability

Supplementary information including details of materials, instruments, experimental procedures, and DFT calculations is available. See DOI: **https://doi.org/10.1039/d5na00686d**.

Acknowledgements

This work was partially supported by Grants-in-Aids for Scientific Research (No. JP23K17945, JP23H03827, and JP24K01552) from MEXT (Tokyo, Japan). In addition, this work is partially based on results obtained from a project, JPNP14004, commissioned by the New Energy and Industrial Technology Development Organization (NEDO). Moreover, this work was partially supported by the Environment Research and Technology Development Fund (JPMEERF20241RA4) of the Environmental Restoration and Conservation Agency provided by Ministry of the Environment of Japan and the Research Grant against Global Warming of the Ichimura Foundation for New Technology. K. Oka also acknowledges support from the Shorai Foundation for Science and Technology, TEPCO Memorial Foundation, Amano Industry Technology Laboratory, Sugiyama Houkoukai, Yamada Science Foundation, Kenjiro Takayanagi Foundation, Kansai Research Foundation for Technology Promotion, Yashima Environment Technology Foundation, JACI Prize for Encouraging Young Researcher, Iketani Science and Technology Foundation, and the Foundation for Interaction in Science & Technology. H. Sei acknowledges support from Takahashi Industrial and Economic Research Foundation, Amano Institute of Technology, Yashima Environment Technology Foundation, JKA and its promotion funds from KEIRIN RACE.

Notes and references

1 O. M. Yaghi, M. O'Keeffe, N. W. Ockwig, H. K. Chae, M. Eddaoudi and J. Kim, *Nature*, 2003, **423**, 705–714.
2 J. R. Li, R. J. Kuppler and H. C. Zhou, *Chem. Soc. Rev.*, 2009, **38**, 1477–1504.
3 B. R. Pimentel, A. Parulkar, E. K. Zhou, N. A. Brunelli and R. P. Lively, *ChemSusChem*, 2014, **7**, 3202–3240.
4 M. Ahlen, O. Cheung and C. Xu, *Dalton Trans.*, 2023, **52**, 1841–1856.
5 L. E. Kreno, K. Leong, O. K. Farha, M. Allendorf, R. P. Van Duyne and J. T. Hupp, *Chem. Rev.*, 2012, **112**, 1105–1125.
6 J. K. Zaręba, M. Nyk and M. Samoć, *Adv. Optical Mater.*, 2021, **9**, 2100216.
7 R. Sakthivel, T. Y. Liu and R. J. Chung, *Environ. Res.*, 2023, **216**, 114609.
8 J. Lee, O. K. Farha, J. Roberts, K. A. Scheidt, S. T. Nguyen and J. T. Hupp, *Chem. Soc. Rev.*, 2009, **38**, 1450–1459.
9 D. W. Lim and H. Kitagawa, *Chem. Rev.*, 2020, **120**, 8416–8467.
10 B.-X. Han, Y.-F. Jiang, X.-R. Sun, Z.-F. Li and G. Li, *Coord. Chem. Rev.*, 2021, **432**, 213754.
11 C. Wang, X. Liu, N. Keser Demir, J. P. Chen and K. Li, *Chem. Soc. Rev.*, 2016, **45**, 5107–5134.
12 J. Canivet, A. Fateeva, Y. Guo, B. Coasne and D. Farrusseng, *Chem. Soc. Rev.*, 2014, **43**, 5594–5617.
13 L. Huang, H. Wang, J. Chen, Z. Wang, J. Sun, D. Zhao and Y. Yan, *Microporous Mesoporous Mater.*, 2003, **58**, 105–114.
14 S. S. Kaye, A. Dailly, O. M. Yaghi and J. R. Long, *J. Am. Chem. Soc.*, 2007, **129**, 14176–14177.
15 P. Küsgens, M. Rose, I. Senkovska, H. Fröde, A. Henschel, S. Siegle and S. Kaskel, *Microporous Mesoporous Mater.*, 2009, **120**, 325–330.
16 F. Yang, H. Huang, X. Wang, F. Li, Y. Gong, C. Zhong and J.-R. Li, *Cryst. Growth Des.*, 2015, **15**, 5827–5833.
17 M. Gorbounov, P. Halloran and S. Masoudi Soltani, *J. CO_2 Util.*, 2024, **86**, 102908.
18 N. C. Burtch, H. Jasuja and K. S. Walton, *Chem. Rev.*, 2014, **114**, 10575–10612.
19 H. Wang, X. Pei, M. J. Kalmutzki, J. Yang and O. M. Yaghi, *Acc. Chem. Res.*, 2022, **55**, 707–721.
20 Z. Mo, D. Tai, H. Zhang and A. Shahab, *Chem. Eng. J.*, 2022, **443**, 136320.

21 N. T. Nguyen, H. Furukawa, F. Gandara, H. T. Nguyen, K. E. Cordova and O. M. Yaghi, *Angew. Chem., Int. Ed.*, 2014, **53**, 10645–10648.
22 K. S. Park, Z. Ni, A. P. Cote, J. Y. Choi, R. Huang, F. J. Uribe-Romo, H. K. Chae, M. O'Keeffe and O. M. Yaghi, *Proc. Natl. Acad. Sci. U. S. A.*, 2006, **103**, 10186–10191.
23 M. Shams, M. H. Dehghani, R. Nabizadeh, A. Mesdaghinia, M. Alimohammadi and A. A. Najafpoor, *J. Mol. Liq.*, 2016, **224**, 151–157.
24 L. Mu, B. Liu, H. Liu, Y. Yang, C. Sun and G. Chen, *J. Mater. Chem.*, 2012, **22**, 12246–12252.
25 J. Yang, Y. B. Zhang, Q. Liu, C. A. Trickett, E. Gutierrez-Puebla, M. A. Monge, H. Cong, A. Aldossary, H. Deng and O. M. Yaghi, *J. Am. Chem. Soc.*, 2017, **139**, 6448–6455.
26 R. Freund, S. Canossa, S. M. Cohen, W. Yan, H. Deng, V. Guillerm, M. Eddaoudi, D. G. Madden, D. Fairen-Jimenez, H. Lyu, L. K. Macreadie, Z. Ji, Y. Zhang, B. Wang, F. Haase, C. Woll, O. Zaremba, J. Andreo, S. Wuttke and C. S. Diercks, *Angew. Chem., Int. Ed.*, 2021, **60**, 23946–23974.
27 K. Zhang, R. P. Lively, M. E. Dose, A. J. Brown, C. Zhang, J. Chung, S. Nair, W. J. Koros and R. R. Chance, *Chem. Commun.*, 2013, **49**, 3245–3247.
28 R. P. Lively, M. E. Dose, J. A. Thompson, B. A. McCool, R. R. Chance and W. J. Koros, *Chem. Commun.*, 2011, **47**, 8667–8669.
29 P. Barbosa, N. C. Rosero-Navarro, F.-N. Shi and F. M. L. Figueiredo, *Electrochim. Acta*, 2015, **153**, 19–27.
30 M. Sadakiyo, T. Kuramoto, K. Kato and M. Yamauchi, *Chem. Lett.*, 2017, **46**, 1004–1006.
31 M. Gao, J. Wang, Z. Rong, Q. Shi and J. Dong, *RSC Adv.*, 2018, **8**, 39627–39634.
32 S. Calero and P. Gómez-Álvarez, *J. Phys. Chem. C*, 2015, **119**, 23774–23780.
33 S. Bhattacharyya, R. Han, W.-G. Kim, Y. Chiang, K. C. Jayachandrababu, J. T. Hungerford, M. R. Dutzer, C. Ma, K. S. Walton, D. S. Sholl and S. Nair, *Chem. Mater.*, 2018, **30**, 4089–4101.
34 F.-F. Lu, X.-W. Gu, E. Wu, B. Li and G. Qian, *J. Mater. Chem. A*, 2023, **11**, 1246–1255.
35 A. Dey, S. K. Konavarapu, H. S. Sasmal and K. Biradha, *Cryst. Growth Des.*, 2016, **16**, 5976–5984.
36 M. P. Suh, H. J. Park, T. K. Prasad and D. W. Lim, *Chem. Rev.*, 2012, **112**, 782–835.
37 P. Lu, Y. Wu, H. Kang, H. Wei, H. Liu and M. Fang, *J. Mater. Chem. A*, 2014, **2**, 16250–16267.
38 M. Dinca, W. S. Han, Y. Liu, A. Dailly, C. M. Brown and J. R. Long, *Angew. Chem., Int. Ed.*, 2007, **46**, 1419–1422.
39 A. Demessence, D. M. D'Alessandro, M. L. Foo and J. R. Long, *J. Am. Chem. Soc.*, 2009, **131**, 8784–8786.
40 H. Hayashi, A. P. Cote, H. Furukawa, M. O'Keeffe and O. M. Yaghi, *Nat. Mater.*, 2007, **6**, 501–506.
41 B. Seoane, J. M. Zamaro, C. Téllez and J. Coronas, *RSC Adv.*, 2011, **1**, 917–922.
42 G.-Y. Hwang, R. Roshan, H.-S. Ryu, H.-M. Jeong, S. Ravi, M.-I. Kim and D.-W. Park, *J. CO_2 Util.*, 2016, **15**, 123–130.
43 A. Huang, H. Bux, F. Steinbach and J. Caro, *Angew. Chem., Int. Ed.*, 2010, **49**, 4958–4961.
44 C. Zhang, R. P. Lively, K. Zhang, J. R. Johnson, O. Karvan and W. J. Koros, *J. Phys. Chem. Lett.*, 2012, **3**, 2130–2134.
45 G. Liu, J. Yang, Y. Zhao and X. Xu, *RSC Adv.*, 2022, **12**, 4408–4416.
46 H. Zhang, M. Zhao, Y. Yang and Y. S. Lin, *Micropor. Mesopor. Mater.*, 2019, **288**, 109568.
47 S. Tardio and P. J. Cumpson, *Surf. Interface Anal.*, 2017, **50**, 5–12.
48 M. Jacquemin, M. J. Genet, E. M. Gaigneaux and D. P. Debecker, *ChemPhysChem*, 2013, **14**, 3618–3626.
49 J. I. Deneff, K. S. Butler, P. G. Kotula, B. E. Rue and D. F. Sava Gallis, *ACS Appl. Mater. Interfaces*, 2021, **13**, 27295–27304.
50 C. Byrne, M. Mazaj and N. Z. Logar, *Mater. Chem. Phys.*, 2025, **332**, 130143.
51 M. J. Kalmutzki, C. S. Diercks and O. M. Yaghi, *Adv. Mater.*, 2018, **30**, e1704304.
52 T. Ami, K. Oka, S. Kitajima and N. Tohnai, *Angew. Chem., Int. Ed.*, 2024, **63**, e202407484.
53 F. Xiang, S. Chen, Z. Yuan, L. Li, Z. Fan, Z. Yao, C. Liu, S. Xiang and Z. Zhang, *JACS Au*, 2022, **2**, 1043–1053.
54 Y. Marcus, *J. Chem. Phys.*, 2012, **137**, 154501.
55 I. Nicotera, V. Kosma, C. Simari, G. A. Ranieri, M. Sgambetterra, S. Panero and M. A. Navarra, *Int. J. Hydrog. Energy*, 2015, **40**, 14651–14660.
56 Y. Ma, J. Liu, W. Yan, X. Li, X. Liu, L. Guo, P. Gong, X. Zheng and Z. Liu, *Microporous Mesoporous Mater.*, 2024, **367**, 112974.
57 Y. X. Lian, S. S. Liu, J. J. Sun, P. Luo, X. Y. Dong, X. F. Liu and S. Q. Zang, *Dalton Trans.*, 2022, **51**, 14054–14058.